

Please cite this article as:

*Tao Zhu,^a Daming Zheng,^a Jiawen Liu,^b Laurent Coolen^b and Thierry Pauporté^{*a}*

PEAI-based Interfacial layer for High Efficiency and Stable Solar Cells Based on MACl Mediated Grown $\text{FA}_{0.94}\text{MA}_{0.06}\text{PbI}_3$ Perovskite

ACS Appl. Mater. Interfaces 12 (2020) 37197–37207

^aChimie ParisTech, PSL Research University, CNRS, Institut de Recherche de Chimie Paris (IRCP), UMR8247, 11 rue P. et M. Curie, F-75005 Paris, France.

^bSorbonne Université, CNRS, Institut de NanoSciences de Paris, INSP, F-75005 Paris, France.

*Corresponding author, email: thierry.pauporte@chimieparistech.psl.eu

KEYWORDS: Perovskite solar cells, Methylammonium formamidinium lead iodide, $(\text{PEA})_2\text{PbI}_4$, Electrical impedance spectroscopy, Interfacial passivation, Charge recombination reduction.

ABSTRACT: Among the 3D organic-inorganic hybrid perovskite (OIHP), mixed formamidinium and methylammonium cations lead iodide is one of the most promising for solar cell application. After optimizing the use of methylammonium chloride (MACl) additive for the preparation of compact, high quality and large crystal grain layers made of pure α -phase perovskite with $\text{FA}_{0.94}\text{MA}_{0.06}\text{PbI}_3$ composition, the treatment of the perovskite surface by a 2-Phenylethylammonium iodide (PEAI) solution has been implemented. This treatment, without any thermal annealing, leads notably to the spontaneous formation of a crystallized $(\text{PEA})_2\text{PbI}_4$ 2D-perovskite nanolayer at the film surface due to partial organic cation dissolution. This buffer layer is shown to favor a fast transfer of the holes towards the HTL and to reduce the recombinations at

and near the perovskite/HTL interface in perovskite solar cells (PSCs). It is shown to boost their maximum power conversion efficiency (PCE) from 20.37% to 22.18% while the hysteresis becomes negligible. A comprehensive study of the device electrical response has been performed. The electrical impedance spectroscopy (EIS) measurements have been fitted with *ad-hoc* equivalent electrical circuits. The electrical responses due to interface stabilization, the intrinsic dielectric relaxation of the perovskite, the charge depletion and charge recombinations have been distinguished. The low frequency capacitance is analyzed as a charge recombination capacitance. The perovskite surface buffer layer is notably shown to suppress charge recombinations from the boosting of the high frequency and low frequency recombination resistances as well as from the marked decrease of the low frequency recombination capacitance. The prepared devices are proved especially resistant to electrical stresses, to light irradiation and to moisture.

1. Introduction

Organic-inorganic hybrid perovskites (OIHPs) are among the most fascinating semiconductor materials due to their versatility, tunability, low temperature preparation and amazing optoelectronic properties.¹ Their direct transition bandgap can be tuned by playing on their composition, they exhibit long charge carrier lifetimes and they can be prepared at low cost starting from precursor solutions which are processed at low temperature.² These compounds are promising for applications in many fields such as photodetectors, lasers, scintillation, LEDs and solar photovoltaics.^{3–18} The latter is of special interest since the power conversion efficiency of solar cells based on OIHP has quickly increased, reaching a present certified record efficiency of 25.2%.¹⁹ OIHP-based solar cells exhibit the highest performance among thin film technologies and their efficiency approaches that of the best silicon technology.

Formamidinium lead tri-iodide (FAPbI₃) perovskite is one of the best suited OIHP materials for perovskite solar cells (PSC) from the point of view of the bandgap for light harvesting of irradiation wavelengths ranging from the near-IR to the near-UV. This compound also allows the generation of a rather large photovoltage output.^{17,18} However, due to the large size of the FA cation, FAPbI₃ is stable at room temperature in its non-perovskite yellow δ -phase which is poorly active in solar cells.²⁰ The stabilization of the photo-active black 3D perovskite α -phase needs the incorporation of extra monovalent cation such as cesium (Cs⁺), rubidium (Rb⁺), methylammonium (MA⁺).... or of their mixture. Another important observation is that the most efficient OIHPs contain methylammonium (MA⁺) as extra organic cation.²¹⁻²⁶ High efficiency and high stability require dense, well-covering, uniform, pin-hole free perovskite layers as well as high phase purity. The OIHP layer must be made of monolithic large crystal grains which go through the entire perovskite thin film.⁹

To increase the performances of PSCs, one must both optimize the OIHP layer and the interfaces with the selective contact layers.²⁷ Complex recipes have been developed for the preparation of high structural quality OIHP layers. Chloride anion additive is known, for a long time, to be beneficial to the formation of large crystal grains and has been used in a large extent in MAPbI₃ perovskite layer synthesis.^{28,29} On the other hand, only a few works have been developed chloride additives for the growth of mixed cation perovskite based on formamidinium and methylammonium.^{22,26,29-31} MA₂Cl solutions were used in several paper for the surface treatment of perovskite films by spin-coating.³³⁻³⁵ Recently, MA₂Cl additive was employed to increase the solubility of GeI₂ and allows the doping of the mixed cation perovskite layer with Ge.³⁶ Mu et al. used MA₂Cl combined with FAI in stoichiometric amounts to obtained mixed Cl and I halide perovskite compounds.³⁰ Kim et al. were the first to employ MA₂Cl as an additive in the perovskite

precursor solution. They successfully produced an intermediate to the pure FAPbI₃ α -phase without annealing.²⁶ Cl ion was proved to stabilize α -phase FAPbI₃ without annealing through enhancing the interactions of FA and I, and reducing the formation energy. The MA ion in the unannealed film caused a total volume shrinkage for the cubic α -phase FAPbI₃ due to the small MA ion size and its large dipole moment, which also reduced the formation energy of α -phase FAPbI₃. However, the methylammonium content must be minimized to reduce the hydrophilicity of the material and its destabilization by degradation/degazing (in CH₃I and NH₃).¹⁸

For the interfaces, the perovskite/hole transporting layer (HTL) one is of utmost importance. The intercalation of an ad-hoc buffer layer enables the fast extraction of holes and their transfer to the HTL. 2-Phenylethylammonium iodide (PEAI) focused our attention since this compounds has been employed for the passivation of the OIHP grain boundaries and surfaces in several works.³⁷ You et al. found that PEAi itself can effectively passivate the perovskite defects and therefore improve the efficiency of the devices.²² PEAi can also form a (PEA)₂PbI₄ 2D-perovskite compound after reaction with I and Pb sources.³⁸

We present PSCs which achieved very high power conversion efficiencies by the engineering of the OIHP precursor solution and interfaces. We used non-stoichiometric precursor solutions in which methylammonium chloride additive acted as a mediator to the growth of dense layers made of large crystal grains. By this technique, a small amount of MA cation was incorporated in FAPbI₃, at the best for the α -phase stability. One of the interests of the presented recipe is that the solution has a rather low concentration of precursor. The technique is also reliable, robust and gives high efficiency with low result dispersion for a large range of additive concentration. The MAcl best molar fraction is found at 48 mol.%. At lower concentration, the OIHP grain size was smaller and more grain boundaries were present. At higher concentration, more recombinations occurred which

mitigated the device fill factor (FF) and open circuit voltage (V_{OC}). We also show that the PEAI treatment without thermal annealing leads notably to the spontaneous formation of $(PEA)_2PbI_4$ perovskite at the surface. It favors a fast transfer of the holes towards the HTL. A comprehensive investigation of the systems by impedance spectroscopy notably shows that recombinations are markedly reduced by using this buffer layer. Overall, the prepared cells were almost hysteresis free. Their power conversion efficiency was greater than 22.1%. The power output of the produced devices was remarkably stable. These PSCs were proved resistant to electrical stresses, to light irradiation and to moisture.

2. Results and discussion

2.1 Perovskite layers description

We have investigated the preparation of OIHP layers from precursor solutions containing a stoichiometric amount of FAI and PbI_2 and various molar fractions of methylammonium chloride additive, namely 40 mol.%, 48 mol.% and 55 mol.%. The related layers are noted MC40, MC48 and MC55, respectively. The precursor concentration was rather low at 1.2 M while a large amount of MAI was employed. The latter was crucial to govern the growth of the perovskite layers. Scanning Electron Microscope (SEM) top-views in **Figure S1(a-c)** (Supporting Information) show that the presence of chloride gradually increased the size of the crystal grains. This anion reduces the density of nucleation seeds and allows the growth of larger grains. The maximum average grain size was close to 1 μm for the MC55 sample (**Figure S1c**, Supporting Information). SEM views of the layer cross-section (**Figure S1d**, Supporting Information) indicated a monolithic structure with the whole thickness of the perovskite layer occupied by single grains.

XRD patterns revealed that the prepared layers were made of ultra-pure cubic α -phase 3D-perovskite. The peaks are indexed in **Figure S2** (Supporting Information) and the layer is textured with the (100) family of plane parallel to the surface. No non-perovskite yellow δ -phase and PbI_2 phase were detected by XRD. The layers were well-crystallized whatever the concentration of additive used. The diffraction peak intensity increased with the additive concentration due to the increase of perovskite grain size. The accurate compositions of the layers were determined by combining EDX and $^1\text{H-NMR}$ techniques. EDX showed that the I/Pb ratio was close to 3 for the three films (**Table S1**, Supporting Information). This technique also indicated that the Cl element was not present or present in a negligible quantity in the final layers. Liquid-state $^1\text{H-NMR}$ allowed us to finely titrate the FA and MA component ratio in the effective perovskite layers employed in the solar cells. The values are reported in **Table S1** (Supporting Information). The interesting result is that x in $\text{FA}_{1-x}\text{MA}_x\text{PbI}_3$ is very low and ranges between 0.061-0.064 (**Table S1**, Supporting Information). This parameter is almost irrespective of the concentration of MACl in the precursor solution. In summary, we can describe the mixed cation perovskite obtained with the various molar fraction of MACl by the 3D perovskite formulae $\text{FA}_{0.94}\text{MA}_{0.06}\text{PbI}_3$.

The absorbance spectra of the layers in **Figure S3a** (Supporting Information) exhibit an absorption edge at about 820 nm which is due to the direct optical transition in $\text{FA}_{0.94}\text{MA}_{0.06}\text{PbI}_3$. The use of pure I as halide permits the extension of the absorption limit in the near-IR. We observed that increasing the MACl % favored the absorbance. It can be related to larger grains and likely to a slight increase of the perovskite layer thickness with MACl additive. **Figure S3b** (Supporting Information) displays the Tauc plots of the absorbance spectra. The linear fit intersection with the energy axis gives an optical bandgap energy (E_g) of 1.53 eV whatever the precursor solution composition. The fact that increasing the MACl concentration does not affect E_g is in good

agreement with a similar organic cation composition of the MC40, MC48 and MC55 layers. In **Figure S3c** (Supporting Information), the normalized photoluminescence (PL) spectra of the various layers overlap. The maximum of the emission was measured at about 811 nm. Time resolved photoluminescence (TRPL) decay curves measured from the layers top are presented in **Figure S3d** (Supporting Information). They were analyzed as described in the Annex 1 of the Supporting Information, using three-exponential decay function. The fit results are gathered in **Table S2** (Supporting Information). The slower component had the best relative contribution (rc) to PL and we assigned it to the bimolecular recombination of the photogenerated charges in the bulk perovskite. The slow decay time is related to the structural quality of the perovskite layers. The longer is this parameter, the higher is the structural quality of the material. From the fits, we measured τ_{slow} at 99 ns, 102 ns and 99 ns for MC40, MC48 and MC55 samples, respectively. The fact that this parameter is not longer for the MC55 layer with the bigger grains shows that the structural quality of the polycrystalline MC55 film was not significantly higher compared to the others. Nevertheless, all the prepared materials exhibited a rather long emission lifetime.

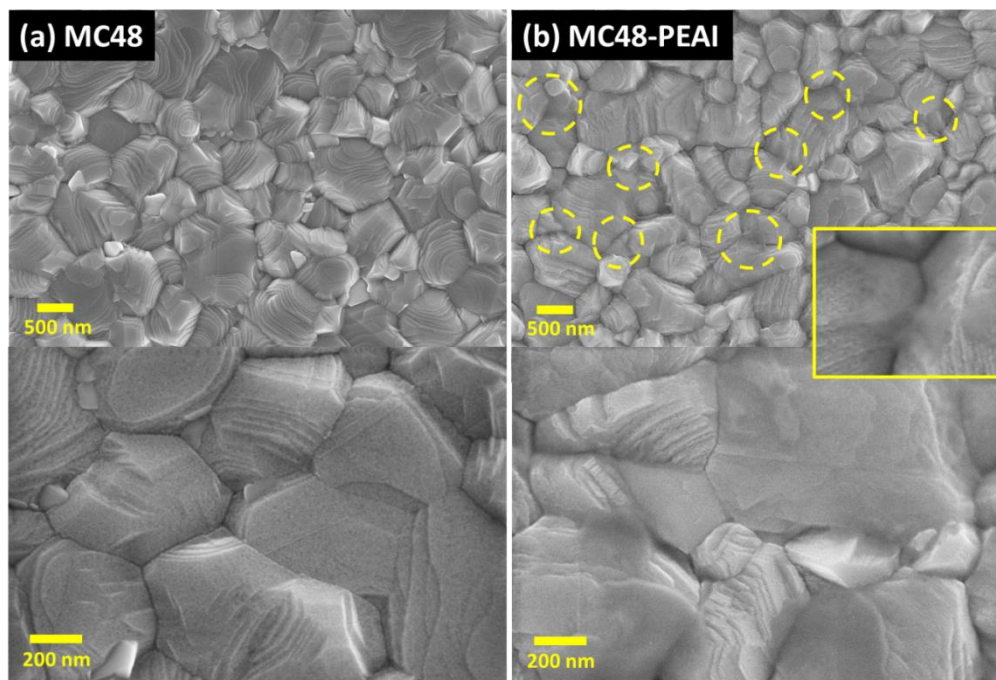


Fig. 1. SEM images of the MC48 perovskite layers surface, (a) before and (b) after the PEAI deposition. Yellow circles are regions where PEAI accumulates. The inset is a zoom view.

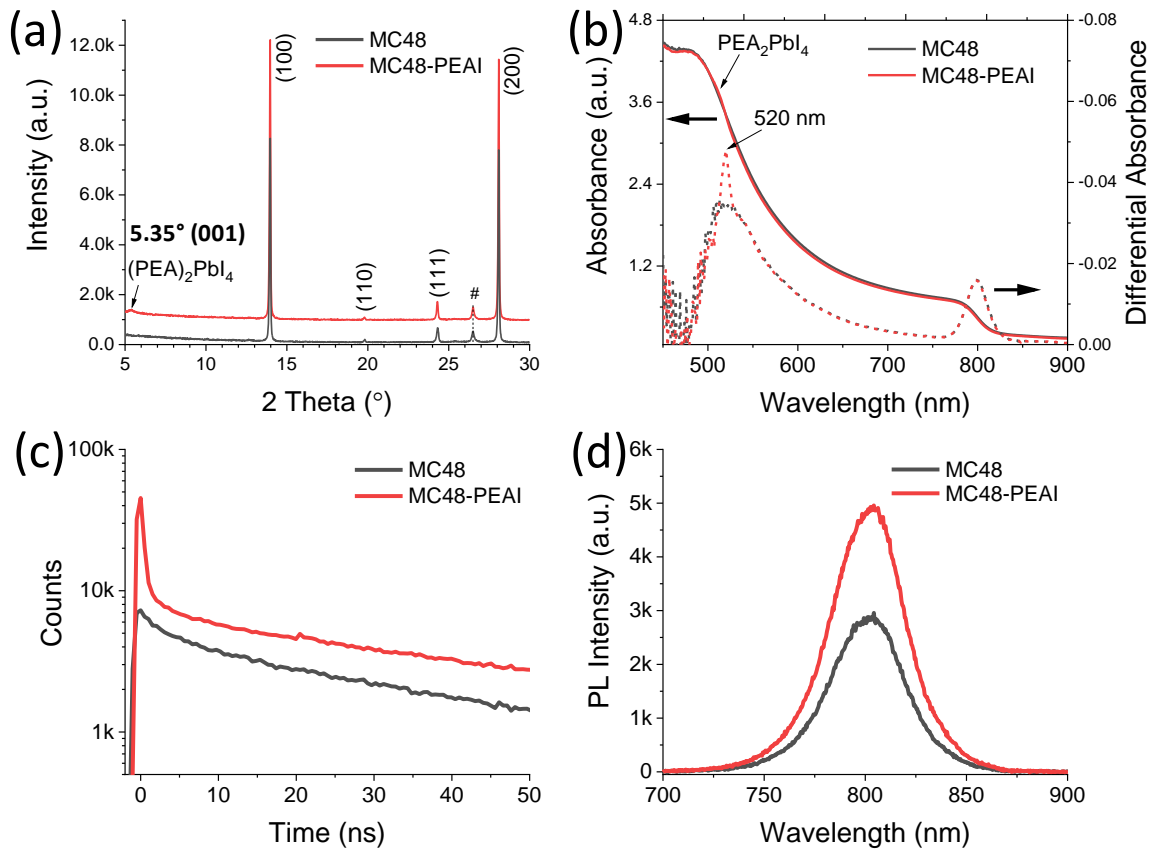


Fig. 2. (a) XRD patterns and (b) absorbance spectra of MC48 and MC48-PEAI layers. (c) TRPL curves and (d) steady PL spectra for pristine and PEAI-treated MC48 samples.

2.2 PEAI treatment

The solar cell study detailed below shows a marked improvement of the PSC performance after the perovskite surface treatment with a 10 mM solution of 2-Phenylethylammonium Iodide (PEAI) in isopropanol (2.49 mg/mL). This treatment was done after the preparation of the perovskite layer and before the HTL deposition. The solution of PEAI was spin-coated on top of the perovskite surface and, importantly, no post-deposition processing was implemented (especially no thermal annealing which is most often done after perovskite surface treatments). On SEM views (**Figure 1**), the PEAI treatment produced a change in the aspect of the perovskite grains surface, especially

of the flat parts of the crystals suggesting a surface modification by a chemical reaction. We also observed the presence of an extra-phase with a haze aspect that accumulated in the deepest zones where most grain (multi-)boundaries are present. On the layer XRD patterns (**Figure 2a**), measured immediately after the PEAI treatment, an extra-peak appeared at an angle of 5.35° which is assigned to the (001) plane of the 2D perovskite with the $(\text{PEA})_2\text{PbI}_4$ composition.²² No PEAI diffraction peak at 4.7° was observed (**Figure S3e**, Supporting Information) therefore no crystallized PEAI was present on the surface at the concentration employed.²² The effect of the PEAI solution concentration was followed and shown in **Figure S3f** (Supporting Information). The 2D peak appeared above 1mg/mL and was clearly present at 2.49 mg/mL, the concentration retained in this study. Its intensity increases with the concentration. We have noted that the presence of crystallized PEAI was detected only for the highest concentration (6 mg/mL). It was then mixed with the 2D phase.

The presence of the 2D perovskite was further confirmed on the absorbance spectra (**Figure 2b**). An absorption edge at 520 nm which corresponds to the near band edge transition in $(\text{PEA})_2\text{PbI}_4$ is revealed in the differential curve (**Figure 2b**). On the TRPL curves (**Figure 2c**), we observed a more intense initial emission for the PEAI treated sample. We also observed a faster initial decay of PL for the treated sample. The latter trend was confirmed on the normalized TRPL curves shown in **Figure S3h** (Supporting Information). **Table S2** (Supporting Information) report that the fast component was much faster for MC48-PEAI (0.47 ns) compared to the untreated MC48 sample (2.8 ns). We explain the initial stronger emission by the fact that the treatment passivates defects near the layer front surface (the irradiated one) and enhances the radiative recombination. However the faster decay is analyzed as an efficient quenching of the radiative recombination by the fast transfer of the hole toward the PEAI-based surface layer. **Table S2** also compares τ_{slow} of the

pristine and treated samples. We measured 100-110 ns for the former sample and about 117 ns after the surface treatment. The improvement was limited because this parameter is sensitive to the perovskite bulk properties, not the surface and near-surface ones. The effect of the treatment on the steady PL spectra of the layers is shown in **Figure 2d**. After the treatment, the PL intensity was stronger due to the stronger emission observed on **Figure 2c**. In summary, a $(\text{PEA})_2\text{PbI}_4$ nanolayer is formed spontaneously on the $\text{FA}_{0.94}\text{MA}_{0.06}\text{PbI}_3$ film surface, without any post-PEAI-deposition thermal annealing treatment. It is assigned to the dissolution of MA and FA cations at the surface by the isopropanol solvent employed and to the higher thermodynamic stability of the 2D compound compared to the 3D one.³⁸ PEAI could remain present in an amorphous state in the deep zones of the perovskite layer. However this deposit looks poorly attached to the perovskite surface and is likely mainly removed upon the Spiro-OMeTAD deposition by spin-coating.

2.3 Perovskite solar cells performances

The solar cell structure is presented in **Figure 3a**. The $\text{FA}_{0.94}\text{MA}_{0.06}\text{PbI}_3$ perovskite layer was contacted by selective contacts: TiO_2 on one side and a spin-coated Spiro-OMeTAD layer on the other side. A gold contact was evaporated on the back of the cell. On the SEM cross-sectional view (**Figure S1d**, Supporting Information), the *mp*- TiO_2 layer thickness was measured at about 130 nm. This layer was soaked with $\text{FA}_{0.94}\text{MA}_{0.06}\text{PbI}_3$. The thickness of the capping pure perovskite layer was about 390 nm. The top Spiro-OMeTAD layer was about 150 nm thick.

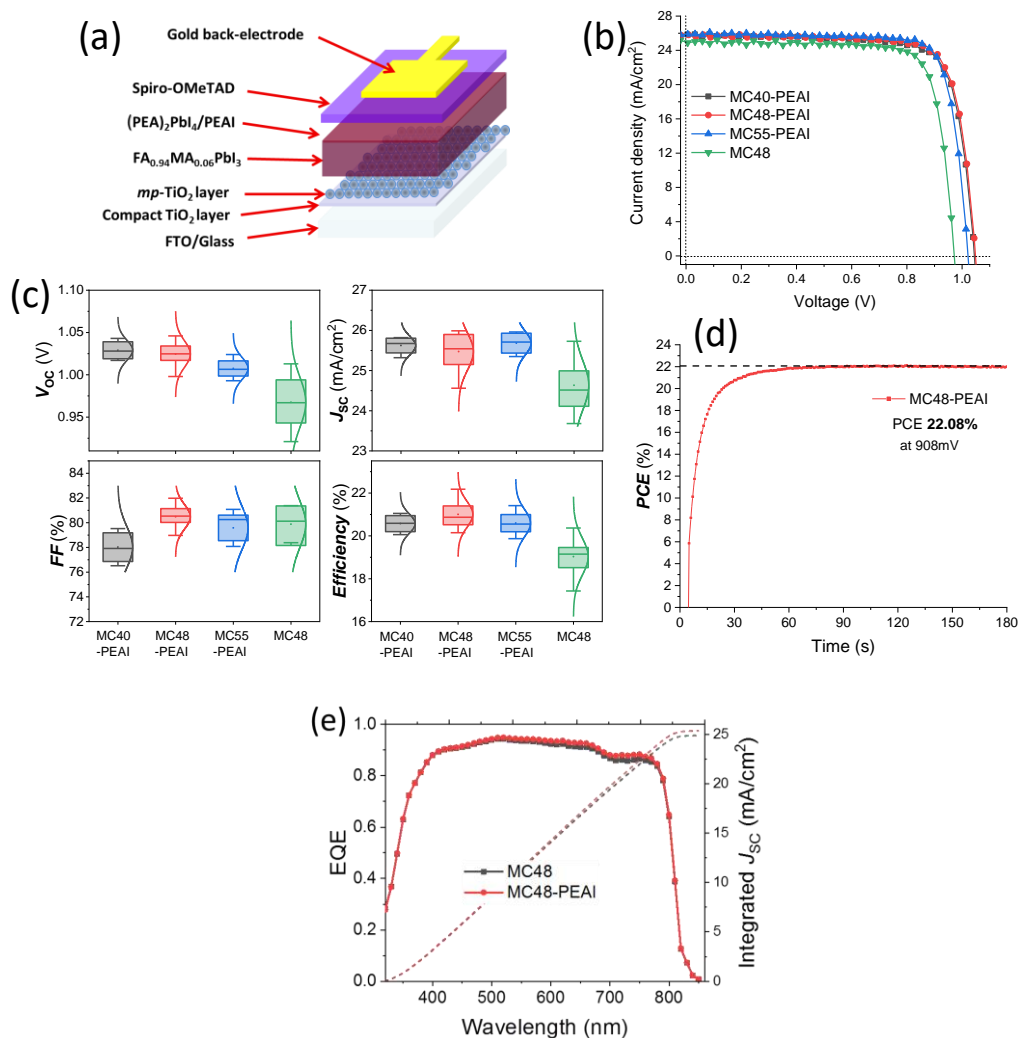


Fig. 3. (a) Device structure employed in the paper with the c -TiO₂/ mp -TiO₂ bottom contact and PEAI-based buffer layer. (b) Typical $J-V$ curves of PSCs prepared with various MACl% with and without the PEAI surface post-deposition treatment. (c) Statistical analysis of the PSC performances and $J-V$ curve parameters. (d) Tracking curve and steady-state PCE of the best cell. (e) EQE spectra of MC48 solar cells with and without PEAI treatment.

The performances of the PSCs were evaluated by measuring their $J-V$ curves under one sun AM 1.5G illumination. The curves of cells prepared with various conditions and with and without PEAI are displayed in **Figure 3b**. **Table 1** gathers the $J-V$ curve parameters of the devices. The hysteresis between the reverse and the forward scans were small due to the low defect density in the perovskite

material and the large grains. We have reproducibly observed that the use of the PEAI treatment increased the cell efficiency. The beneficial effect was found on both the short circuit current, J_{SC} , and on the open circuit voltage, V_{OC} , parameters. The higher J_{sc} with the treatment is in agreement with the TRPL results detailed above. The PEAI-passivation surface nanolayer dramatically reduces the non-radiative recombination by passivating the perovskite surface defects. Moreover, the hole charge are quickly separated by transfer to the nanolayer and it reduces the charge recombination in the perovskite. This fast charge transfer is beneficial of the solar cell current generation. The V_{OC} is increased significantly with the PEAI treatment due to surface defects passivation and reduction of the interfacial charge recombinations. This point will be confirmed in Section 2.4 by the electrical impedance spectroscopy (EIS) study. In average, the post-deposition treatment boosted the PCE by about 10%. Another beneficial effect of the treatment is the reduction of the hysteresis (**Table 1**).

Table 1 Photovoltaic J - V parameters of best $\text{FA}_{0.94}\text{MA}_{0.06}\text{PbI}_3$ cells prepared with various MACl %, with and without the PEAI surface post-deposition treatment (under AM 1.5G conditions, $100 \text{ mW}\cdot\text{cm}^{-2}$).

Cell	Scan direction	V_{oc}/V	$J_{sc}/\text{mA}/\text{cm}^2$	$FF/\%$	$PCE/\%$	$HI^a/\%$
MC40-PEAI	Reverse	1.046	25.83	77.69	21.00	3.2
	Forward	1.035	25.82	76.10	20.33	
MC48-PEAI	Reverse	1.060	25.94	80.62	22.18	3.7
	Forward	1.052	25.93	78.26	21.35	
MC55-PEAI	Reverse	1.024	25.90	80.75	21.41	4.5
	Forward	1.014	25.93	77.77	20.44	
MC48	Reverse	1.002	24.73	82.3	20.37	4.5
	Forward	0.994	24.47	80.02	19.46	

^a HI : Hysteresis index defined as $[\text{PCE}(\%)_{\text{rev}} - \text{PCE}(\%)_{\text{for}}] / \text{PCE}(\%)_{\text{rev}}$

MACl additive molar fraction has also a significant effect on the cell electrical properties. In **Table 1**, J_{sc} is the highest for MC48-PEAI and MC55-PEAI and the best V_{OC} is achieved by MC48-PEAI.

Overall, the best power output was reached for the MC48-PEAI devices. The improvement between MC40-PEAI and MC48-PEAI cells can be explained by larger grains and higher structural quality. The V_{OC} parameter depends on the recombination rate, especially on the recombinations at and near the perovskite/selective contact interfaces. The lower efficiency of the MC55-PEAI cells compared to the MC48-PEAI ones is the effect of lower FF and V_{oc} . We will show in Section 2.4 that these components are related to the internal resistances of the devices which are themselves related to the charge recombinations. We can conclude that MC55-PEAI are not the best devices due to a lower quality of the interfaces.

Overall, choosing MACl at 48mol.% appears as the best choice for the best performances. The observation made for the best cells were confirmed by the statistics of the $J-V$ curve parameters distribution (**Figure 3c**). The large grains, high crystallinity and high absorbance over a large visible-near infrared range of the produced perovskite layers gave rise to high performances. We have also noted that the PEAI treatment especially boosts the J_{SC} and the V_{OC} of the cells by improving the perovskite/HTM interface, reducing the surface defects and favoring the fast charge transfer towards the selective contact. It also reduces the PCE dispersion. **Table 1** shows that the best PCE was measured at 22.18%. This cell had a hysteresis index of only 3.7%. Importantly, this device was tracked at its maximum power output. It reached a stabilized efficiency of 22.08% after about 80s. This value is very close to the measurement on the reverse scan (**Figure 3d**).

The ability of the cells to collect light over a large wavelength range and to generate charge with a high efficiency was confirmed by measuring their EQE spectra. The effect of PEAI on the EQE spectrum is presented in **Figure 3e**. EQE was enhanced with the treatment over the whole visible range. It augmented the J_{sc} obtained by curve integration from 24.8 mA.cm⁻² to 25.1 mA.cm⁻². It confirms that the treatment favors the charge generation and charge extraction at the

perovskite/HTL interface. **Figure S3g** (Supporting Information) shows the effect of the MAI molar fraction on the EQE spectra. By integrating the curves, J_{SC} as high as $25.4 \text{ mA}\cdot\text{cm}^{-2}$ were calculated ($24.9 \text{ mA}\cdot\text{cm}^{-2}$, $25.1 \text{ mA}\cdot\text{cm}^{-2}$ and $25.4 \text{ mA}\cdot\text{cm}^{-2}$ for MC40-PEAI, MC48-PEAI and MC55-PEAI, respectively) and were in good agreement with the J - V curve data.

We also performed the analysis of the V_{OC} as a function of the white light illumination power density. The curves with and without PEAI treatment are presented in **Figure 4a**. For the investigated cells, the V_{OC} was superior over all the light intensity range after the PEAI treatment. The V_{OC} scaled logarithmically with the light power density (I) and followed the relationship:

$$qV_{OC} = E_g + n_{ID}kT \ln(I/I_0) \quad (1)$$

with q the elementary charge, k the Boltzmann constant, T the absolute temperature and n_{ID} the ideality factor. The latter parameter is related to the main recombination phenomena occurring at the V_{oc} .³⁹ We found $1.40 < n_{ID} < 1.50$ for matured cells (cells stored several days in N_2 atmosphere) (**Figure 4**). A smaller slope was found after the PEAI treatment (**Figure 4a**). It is known that deviation of n_{ID} from 1 reflects the occurrence of defect-assisted recombination in the PSCs. n_{ID} values suggest that, at the open circuit, a Shockley-Read-Hall (SRH) recombination mechanism through perovskite intragap defects is the dominating recombination process at the V_{oc} . We have observed that, like in the case of MAPbI_3 perovskite,³⁹ n_{ID} increases with aging and SRH recombination increases with this parameter.

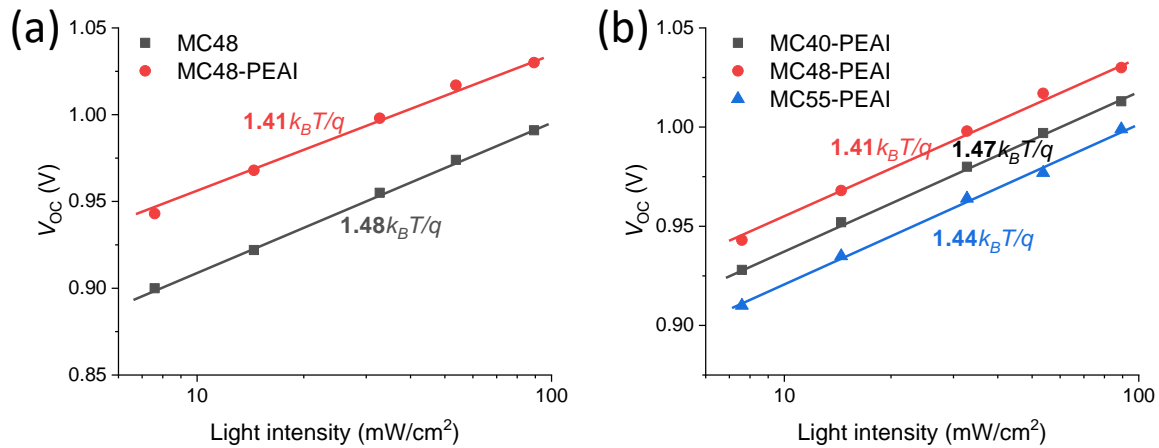


Fig. 4. V_{oc} versus light intensity (power density) curves. (a) MC48 cells with and without PEAI treatment. (b) Effect of MACl%. The curve slopes provide the ideality factor, n_{ID} , values (numbers in bold).

2.4 Impedance spectroscopy study of the PSCs

To gain further insight into the cell functioning, the effect of the buffer layer and cell maturation, we have studied the solar cells by EIS. This characterization technique is performed *in operando*, is safe for the device and provides fruitful information on its functioning.⁴⁰⁻⁴⁴ The PSCs have been investigated under white light irradiation with a power density of about 0.9 sun. The applied voltage (V_{appl}) was varied between the short circuit and the open circuit conditions.

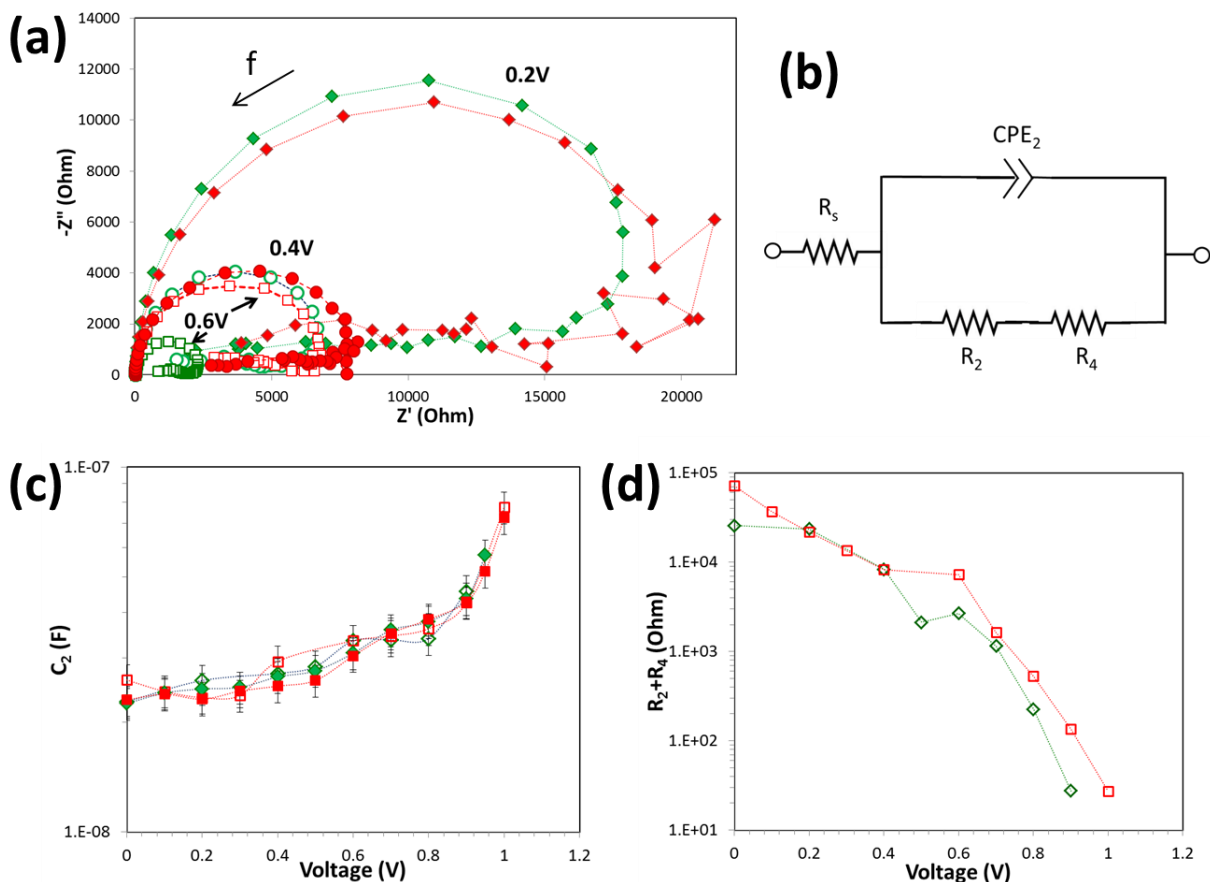


Fig. 5. (a) Impedance spectra of MC48 and MC48-PEAI solar cells measured at various applied voltages. Green symbols: MC48; Red symbols: MC48-PEAI. (b) Equivalent electrical circuit used to fit the high frequency part of the spectra. (c) C_2 parameter of fresh and matured cells. (d) R_2+R_4 parameter of fresh cells. (c) & (d) symbols: green diamonds = MC48 cell, red squares = MC48-PEAI cell; open symbols = fresh cells; full symbols = matured cells (stored several days in a N_2 -filled glovebox).

The Nyquist plots (imaginary part versus the real part of the complex impedance) of fresh cells polarized at various applied voltages and which underwent or not the PEAI treatment are presented in **Figure 5a**. Their shape was rather unusual for solar cells under illumination.¹⁷ At high frequencies ($f > 50$ -150 Hz), a circle arc was found. After an inductive transition at intermediate frequency, a special behavior was found that cannot be fitted with a classical electrical circuit. The imaginary part of the impedance was negative but was pinned, remaining almost constant over a

large frequency range, while at the same time, the real part of the spectra decreased as the frequency decreased. We have focused our analysis on the circle arc at $f > 50$ -150 Hz. It was fitted with the equivalent electrical circuit (EEC) shown in **Figure 5b**. We have employed in this paper the same notation as in the general EEC for the analysis of PSC impedance spectra presented in our previous work⁴⁰ and shown in **Figure S4a** (Supporting Information). R_s is a series resistance measured at high frequencies which is due to the contacts and wires. The flattened circle arc was fitted by a constant phase element (CPE) in parallel with a resistance. The CPE impedance (Z_{CPE}) varies as $Z_{CPE} = \frac{1}{T(i\omega)^p}$ in the complex plane. ω notes the angular frequency. It is related to the frequency as $f = \frac{\omega}{2\pi}$. i is $\sqrt{-1}$, and p is a number lower than 1. We have extracted the capacitances values from the Z_{CPE} parameters by the approach described by Brug et al.^{16,17,40,43,44} The formulae employed and the analysis protocol are more detailed in the **Annex 2: Analysis of the impedance spectra** of the Supporting Information. C_2 versus V_{appl} of fresh cells is displayed as open symbols in **Figure 5c**. C_2 is assigned to the intrinsic dielectric relaxation capacitance of the perovskite and to a depletion capacitance above 0.7V. We show below that its behavior is unchanged with the cell aging. Therefore, the bulk perovskite did not evolve during the first days of the PSC life. The resistance measured was quite large and, based on the general EEC,⁴⁰ is assigned to the sum of two recombination resistances, R_2 and R_4 . The large values result from the domination of the R_4 parameter. The special low frequency behavior of the cell can be assigned to the interfacial reactivity and slow processes that occur at the interfaces. Perovskite/selective contacts Interfaces in fresh cells would not be stabilized either for the pristine or PEAI-treated cells.

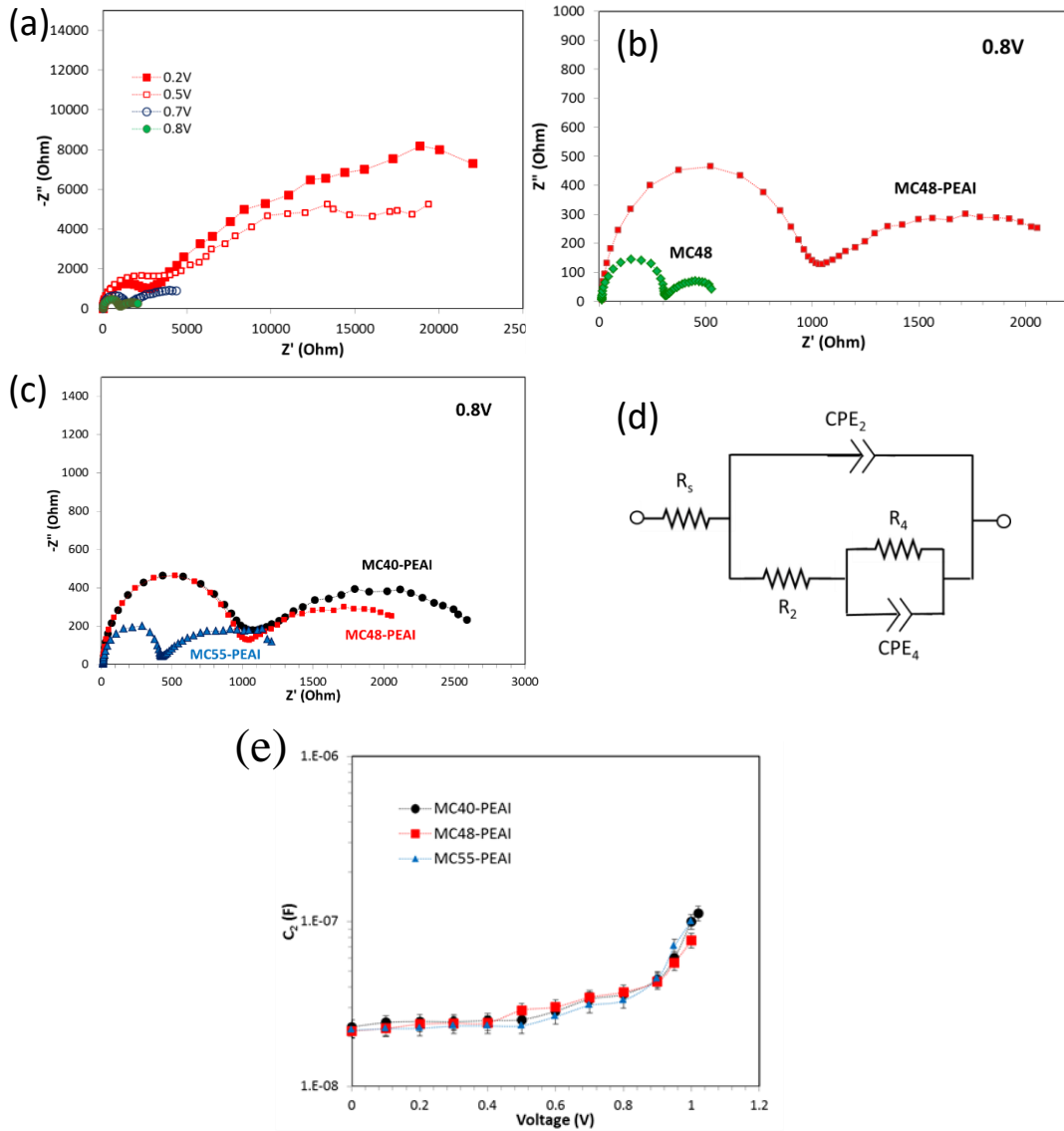


Fig. 6. Nyquist plots of the EIS spectra. (a) Effect of the applied voltage on a 7 days old MC48-PEAI cell. (b) Effect of PEAI (MC48 and MC48-PEAI, $V_{\text{appl}}=0.8\text{V}$); (c) Effect of MACl (PEAI-treated cells, $V_{\text{appl}}=0.8\text{V}$) and (d) Electrical equivalent circuit used to analyze the data. (e) Effect of MACl molar fraction on C_2 parameter versus the applied voltage.

Further characterizations of the PSCs were carried out after their aging for a few days in a N_2 filled glovebox (typically 6-7 days). This maturation period of the solar cells results in an increase of the overall efficiency of the PSC mainly due to the increase of the V_{oc} and of the J_{sc} in a less extend as shown in **Table S3** (Supporting Information). After this period of time, the Nyquist plots exhibited

two main relaxations as shown in **Figure 6a-c**. It suggests that during the maturation, reactions occurred that results in the stabilization of the low frequency signal. These spectra have been fitted with the EEC presented in Figure 6d and also derived from the general EEC. **Figure 6a** presents the effect of applied voltage on the Nyquist impedance plot. When the voltage was increased, the two circle arcs were reduced in size due to a reduction of both R_2 and R_4 resistance as schematically displayed in the **Annex 2** (Supporting Information). **Figure 6b** reports impedance spectra of a pristine and a PEAI-treated cells. The amplitude of the circles was increased by the treatment and therefore R_2 and R_4 were increased. **Figure 6c** shows that the amplitude of the circle arcs also varied with the MAI molar fraction employed to prepare $\text{FA}_{1-x}\text{MA}_x\text{PbI}_3$. To quantify these changes, the spectra were fitted using the simplified EEC presented in **Figure 6d**. Due to the appearance of a second circle arc, we added a CPE capacitive element, noted CPE_4 , in parallel with R_4 in the EEC of **Figure 5b**. C_4 capacitance values were extracted from CPE_4 as detailed in the annex 2 (Supporting Information). No inductive loop was found and we stopped the analysis at 0.1 Hz since at lower frequency, the signal could be rather noisy.

C_2 is a light insensitive element.¹⁷ **Figure 5c** and **Figure 6e** show that this parameter remained the same with a battery of changed parameters: the cell age, the PEAI treatment and the MAI additive fraction in the perovskite precursor solution. The curves were similar over the whole investigated applied voltage range. Below 0.5V, this capacitance remained almost constant. It is assigned to the intrinsic dielectric relaxation of the perovskite.^{17,40} The composition of the perovskite of the various cells is about the same, consequently this parameter did not vary significantly in **Figure 5c**. Above 0.6 V, C_2 increased due to a charge storage effect. At high V_{appl} , C_2 is dominated by the capacitance due to the charge stored in a depleted region at the TiO_2 /perovskite layers. In the literature, the depleted region has been described as mainly extending either in the titania layer and/or in the

doped perovskite layer.^{41,45,46} The Mott-Schottky plot of C_2 in **Figure S4** (Supporting Information) results in a linear section. The linear fits extrapolate at the same potential for the various cells, between 1.08V-1.12V. It has been assigned to the built-in potential (V_{bi}) in the literature.⁴⁷

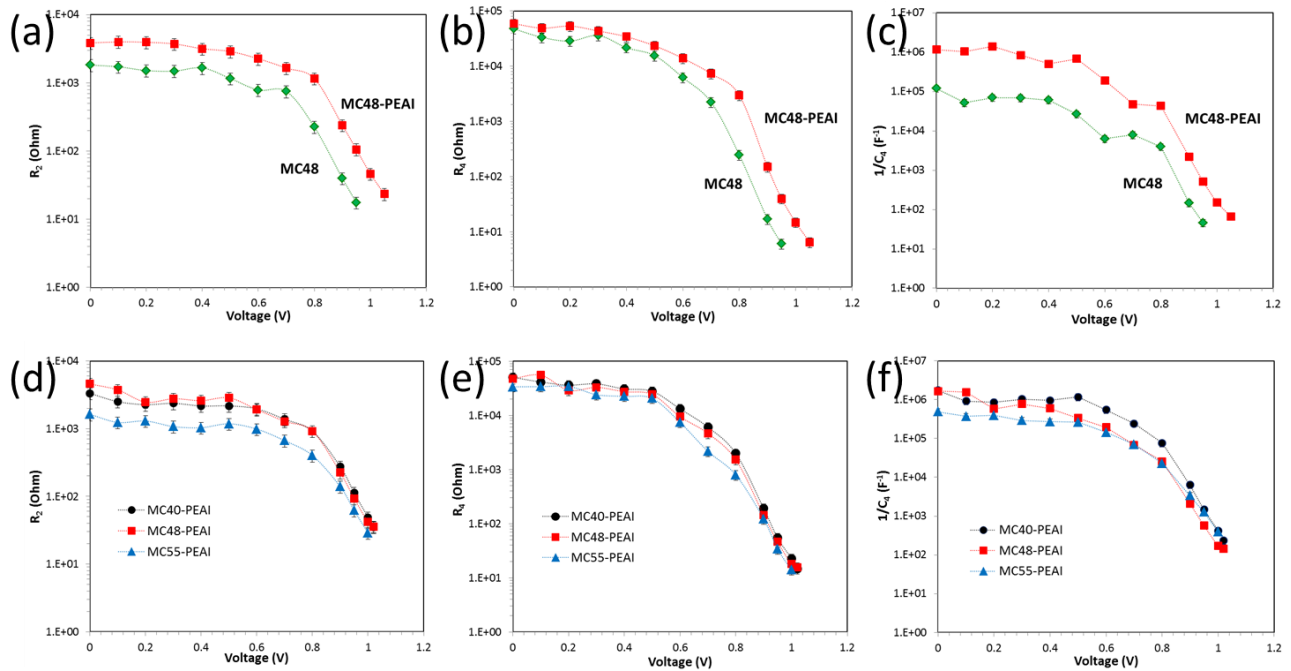


Fig. 7. (a-c) Effect of PEAI treatment on the impedance spectra parameter versus V_{app} . (a) R_2 ; (b) R_4 and (c) $1/C_4$. Effect of MAI additive molar fraction: (d) R_2 ; (e) R_4 ; and (f) $1/C_4$.

The other electrical elements, R_2 , R_4 and C_4 were light sensitive and we will see that all of them are related to charge recombination phenomena. For R_2 , the PEAI treatment results in a significant increase of this parameter (**Figure 7a**). A consequence is that, above 0.7V, it shifts the resistance to higher potential. The same behavior was found for R_4 which is also a recombination resistance. Recombination resistances are inversely related to the recombination rate and they provide a direct quantitative view of the recombination processes. The higher is this resistance, the lower is the

recombination rate. The fact that the PEAI nanolayer shifts R_2 and R_4 curves toward higher voltage is favorable for the cell performances since it increases the cell V_{OC} .

C_4 is a light sensitive parameter which value dramatically increases with the light irradiation and can reach very high values. In our case, at high V_{app} , C_4 attained 1.10^{-1} F.cm⁻². There is little doubt that C_4 is also related to recombination of charges. Because charge recombinations in PSC are a phase delayed phenomenon, in addition to the real component, an imaginary component is also introduced. This imaginary component is analyzed here as a capacitance in the equivalent electrical circuits used to fit our data (**Figures 6d**). It is the main contribution of C_4 . This delayed recombination process is a particular behavior occurring in PSCs due to the ionic conductivity of the perovskite. The movements of ions introduce defects that act as recombination centers and affect the dynamics of the charges. In **Figures 7a-c**, the three parameters R_2 , R_4 and $1/C_4$ clearly appear as related since they exhibit a similar behavior. We can also note that their shape reproduces the J - V curve shape since the $R_s+R_2+R_4$ sum is the total resistance of the devices at the steady state. These three parameters increased markedly with the PEAI treatment which passivates the interfacial defects, favors the hole transfer toward the HTL and lower the recombination phenomena. Therefore, higher J_{SC} and V_{OC} are achieved when the treatment is done (**Figure 3**).

Figure 7 shows some differences in the electrical behavior of cells prepared with various MACl additive fraction contents. The main one is the marked lowering of the R_2 parameter for the MC55-PEAI cells. R_4 and $1/C_4$ are also slightly lower. We can conclude that more recombinations occurred in these cells especially at high voltage. The surface of the MC55 film was more defective and the passivation was less effective for these cells. Consequently, the FF and V_{OC} were the most impacted parameters which were significantly reduced at the high MACl molar fraction (**Figure 3c**). Because of the ion mobility in the perovskite and the dynamics of defect formation and repair

described, it is rather difficult to go further in the analysis and assigned a sound origin for R_2 and R_4 . However in Figure 7, we remark that the behaviour of $1/C_4$ is similar to that of R_2 which lead us to tentatively assign the later resistance to recombination occurring in the bulk, likely near the interface because this element is sensitive to the surface treatment. On the other hand, R_4 would be an interfacial recombination resistance.

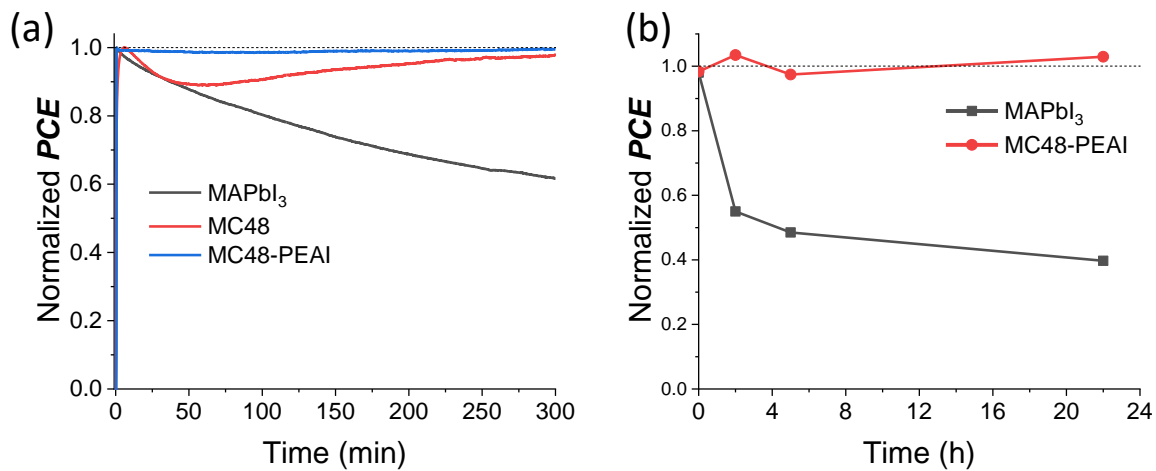


Fig. 8. (a) Tracking of MAPI, MC48 and MC48-PEAI solar cell normalized power outputs under continuous one sun AM1.5G illumination (unencapsulated devices, 45% RH). (b) Normalized PCE evolution of MC48-PEAI and MAPI unencapsulated cells upon storage in a chamber with a 90% RH.

2.5 Operational stability of the devices

Developing highly stable PSCs that are resistant to moisture, light and electrical stresses is a great challenge for the future of this technology. We have performed several experiments which have demonstrated the high stability of the PSCs developed in this study. Impedance spectroscopy is a stressing operating mode for the cells. The operated devices are then submitted to a continuous light irradiation, to various applied voltages and to a superimposed ac stimulus. The full characterization of a solar cell by EIS lasts more than one hour. For each cell investigated, we controlled their stability by measuring their $J-V$ curves before and after the EIS characterization.

Results for some of them are gathered in **Table S4** (Supporting Information). The performances of the pristine and of the PEAI-treated devices were slightly higher after EIS characterizations due to a better V_{OC} . The prepared devices presented a high robustness and they met the stability requirement for reliable EIS characterizations as defined by one of us in Ref.⁴²

The stability was also followed for 5 hours under a continuous one sun AM 1.5G illumination and at a relative humidity (RH) of 45%. **Figure 8a** compares the pristine and the PEAI-treated unencapsulated MC48 cells with a MAPI unencapsulated cell. The latter was preferred to a pure FAPI cell due to the fact that the FAPI perovskite in its α -phase is unstable and quickly decomposes in its non-photoactive δ -phase. The power output slightly decreased and then increased for the pristine cell while it was highly stable and unchanged for the PEAI-treated one. On the other hand, the MAPI cell power output continuously decreased during the same test. The stability against moisture was tested by storing the unencapsulated cells in a chamber with a 90% RH and ambient light condition (**Figure 8b**). The power output was stable for 20h for the MC48-PEAI cell. At the same time, the MAPI cell was not stable, losing rapidly 60 % of its PCE within only 20h. The variations of the $J-V$ curve parameters are shown in **Figure S5** (Supporting Information).

3. Conclusions

We have developed the use of methyl ammonium chloride as an additive in rather low concentration mixed organic cation precursor solutions. MACl is shown to mediate the growth of the layers. The resulting films were uniform, compact, with no pinholes and made of remarkably large size perovskite crystal grains. By this technique, a small amount of MA cation was incorporated in $FAPbI_3$, stabilizing the pure α -phase with $FA_{0.94}MA_{0.06}PbI_3$ composition. The excess was removed by sublimation and degradation. The presented growth technique is reliable,

robust and gives devices efficient over a large range of additive concentration. The best MACl molar fraction is found at 48mol.%. To further increase the PCE of the solar cells, a treatment with a PEAI solution has been implemented. This treatment, without any thermal annealing step, leads to the spontaneous formation of (PEA)₂PbI₄ perovskite at the surface. This buffer layer has been shown to favor a fast transfer of the holes towards the HTL and to reduce the recombinations at the perovskite/HTL interface. Overall, the optimized devices had a PCE higher than 22.1%. A comprehensive investigation of the systems by impedance spectroscopy has been carried out. The change in the impedance spectra within the first days of the device storage corresponds to a maturation step which involves reactions at the interface(s). The high frequency capacitance was irrespective of the PSC age and treatment was assigned at low V_{appl} to the intrinsic dielectric relaxation of the perovskite. The high frequency resistance R_2 and R_4 were analyzed as recombination resistances and C_4 as a recombination capacitance. Furthermore, our results indicate that R_2 and C_4 are likely related to recombination centers localized near the interface whereas R_4 would correspond to an interfacial recombination resistance. Overall, the variations of R_2 , R_4 and $1/C_4$ explain the variations in FF and V_{OC} of the PSCs with the MACl mol.% and the PEAI treatment. The power output of the produced devices was remarkably stable. These PSCs were proved resistant to electrical stresses, to light irradiation and to moisture.

4. Experimental Section

The full experimental details are given at the beginning of the Supporting Information. The fluorine-doped SnO₂ (FTO) substrates (TEC 7 from Pilkington) were patterned, etched and cleaned as described in our previous Ref.²⁷. The compact TiO₂ layer, noted *c*-TiO₂, was deposited by spray pyrolysis and the spin-coated mesoporous (*mp*-TiO₂) were deposited as described in our previous works.^{16,27,48}

T. Zhu, D. Zheng, J. Liu, L. Coolen, Th. Pauporté, *ACS Appl. Mater. Interfaces* 12 (2020) 37197–37207

A mixed cation precursor solution with a 1.2M concentration was prepared by mixing 206 mg of formamidinium iodide (FAI, greatcell), 553 mg of PbI_2 (TCI), and 32.4 mg, 38.9 mg and 44.6 mg (which represent 40 mol.%, 48 mol.% and 55 mol.% of precursor solution PbI_2 content, respectively) of methylammonium chloride (MACl, Alfa aesar) in 800 μL DMF and 200 μL DMSO. The solutions was spin-coated as described in the Supporting Information to form films which were annealed at 153 °C for 13 min. These films and the corresponding solar cells are noted MC40, MC48 and MC55. The PEAI post-deposition treatment consisted in dropping 60 μL of a 10 mM 2-Phenylethylamine Hydroiodide (PEAI) solution (2.49 mg in 1 mL of isopropanol) onto the perovskite layer. A one-step spin-coating program was employed: 2000 rpm/s acceleration, 3000rpm for 20s.

The Spiro-OMeTAD (Borun New Material Technology) film and the gold back-contact were prepared as described in Ref.²⁷ Unless specified, the solar cells where matured by storing them several days in a N_2 glovebox before to be characterized.

The J - V curves were measured as described in Ref.²⁷ using AM 1.5G illumination conditions (100 mW/cm^2)⁴⁹ calibrated with help of a reference silicon solar cell.⁵⁰ The XRD patterns, the absorbance and photoluminescence spectra were measured as described in Ref.²⁷ and in the Supporting Information. The samples were observed with a high resolution Ultra 55 Zeiss FEG field-emission scanning electron microscope (FE-SEM) operated in the in-lens mode. The EDX spectra were measured with a Quantax system from Bruker operated at 15 kV.

^1H -NMR spectra were recorded on a Bruker Avance 500 MHz Neo spectrometer. Chemical shifts were measured in ppm using the residual DMSO solvent signal as internal reference. Perovskite layers deposited on a sprayed c - TiO_2 layer were dissolved in DMSO- d_6 solvent (99.96 %D,

H₂O<0.01%, Euriso-top) and the NMR spectra of the solutions were measured. These solutions were highly stable.

The time-resolved photoluminescence (TRPL) curves were measured as detailed in Ref.⁴³ and in the Supporting Information. The electrical impedance spectra between 1 MHz and 100 mHz, were measured at room temperature by a PGSTAT 12 equipment from Autolab. The AC signal was 20 mV. Voltages (V_{appl}) were applied between the short circuit and the open circuit. An halogen Schott lamp was employed to provide a light power density of ~ 0.9 sun. The cell illuminated area was 0.16 cm² defined by a mask. All the measured cells had the same contact/illumination geometries. The Z-view software from National Instrument was employed for the spectra analysis.

ASSOCIATED CONTENT

Supporting Information to this paper can be found online. SEM view of the layers and of a solar cell; XRD patterns of the FA_{0.94}MA_{0.06}PbI₃ layers; perovskite layers titration; Absorbance and Tauc plot of the layers; PL spectra and TRPL curves of the layers; Effect of PEAI treatment on the perovskite layer XRD; EQE curves of the solar cells; TRPL curve analysis, decay times and their relative contribution; General equivalent electrical circuit of a perovskite solar cell under illumination; Mott-Schottky plots; Analysis of the impedance spectra; *J-V* curve parameters before and after EIS study of the PSCs; Stability measurement by *J-V* curve parameters tracking.

AUTHOR INFORMATION

Corresponding Author

* thierry.pauporte@chimieparistech.psl.eu

Authors Contributions

Tao Zhu: Conceptualization, Investigation, Data analysis, Writing; **Daming Zheng:** Investigation, data analysis, Writing; **Jiawen Liu:** Investigation; Laurent Coolen, Data analysis, reviewing; **Thierry Pauporté:** Supervision, Data analysis, Writing, Reviewing and Editing.

Notes

The authors declare no competing interests.

ACKNOWLEDGMENT

Dr. Marie-Noelle Rager (NMR-Facility, Chimie-Paristech, France) is acknowledged for NMR measurements. Mrs Fei Cheng (IRCP, Chimie-paristech, France) is acknowledged for experiments and drawing of Figure S3f. T.Z. and D.Z. thank the CSC-Paristech and CSC programs for Ph.D scholarships. The ANR agency is acknowledged for financial support (Moreless project ANR-18-CE05-0026).

REFERENCES

- (1) Saparov, B.; Mitzi, D. B. Organic–Inorganic Perovskites: Structural Versatility for Functional Materials Design. *Chem. Rev.* **2016**, *116*, 4558–4596.
- (2) Leblanc, A.; Mercier, N.; Allain, M.; Dittmer, J.; Pauporté, T.; Fernandez, V.; Boucher, F.; Kepenekian, M.; Katan, C. Enhanced Stability and Band Gap Tuning of α -[HC(NH₂)₂]PbI₃ Hybrid Perovskite by Large Cation Integration. *ACS Appl. Mater. Interfaces* **2019**, *11*, 20743–20751.

- (3) Veldhuis, S. A.; Boix, P. P.; Yantara, N.; Li, M.; Sum, T. C.; Mathews, N.; Mhaisalkar, S. G. Perovskite Materials for Light-Emitting Diodes and Lasers. *Adv. Mater.* **2016**, 28, 6804–6834.
- (4) Kim, H. S.; Lee, C. R.; Im, J. H.; Lee, K. B.; Moehl, T.; Marchioro, A.; Moon, S. J.; Humphry-Baker, R.; Yum, J. H.; Moser, J. E.; Grätzel, M.; Park, N. G. Lead Iodide Perovskite Sensitized All-Solid-State Submicron Thin Film Mesoscopic Solar Cell with Efficiency Exceeding 9%. *Sci. Rep.* **2012**, 2, 591.
- (5) Lee, M. M.; Teuscher, J.; Miyasaka, T.; Murakami, T. N.; Snaith, H. J. Efficient Hybrid Solar Cells Based on Meso-Superstructured Organometal Halide Perovskites. *Science* **2012**, 338, 643–647.
- (6) Liu, M.; Johnston, M. B.; Snaith, H. J. Efficient Planar Heterojunction Perovskite Solar Cells by Vapour Deposition. *Nature* **2013**, 501, 395–398.
- (7) Burschka, J.; Pellet, N.; Moon, S. J.; Humphry-Baker, R.; Gao, P.; Nazeeruddin, M. K.; Grätzel, M. Sequential Deposition as A Route to High-Performance Perovskite-Sensitized Solar Cells. *Nature* **2013**, 499, 316–319.
- (8) Zhang, J.; Barboux, P.; Pauporté, T. Electrochemical Design of Nanostructured ZnO Charge Carrier Layers for Efficient Solid-State Perovskite-Sensitized Solar Cells. *Adv. Energy Mater.* **2014**, 4, 1400932.
- (9) Nie, W.; Tsai, H.; Asadpour, R.; Blancon, J. C.; Neukirch, A. J.; Gupta, G.; Crochet, J. J.; Chhowalla, M.; Tretiak, S.; Alam, M. A.; Wang, H. L. High-Efficiency Solution-Processed Perovskite Solar Cells with Millimeter-Scale Grains. *Science* **2015**, 347, 522–525.
- (10) Zhang, J.; Juárez-Pérez, E. J.; Mora-Seró, I.; Viana, B.; Pauporté, T. Fast and Low Temperature Growth of Electron Transport Layers for Efficient Perovskite Solar Cells. *J. Mater. Chem. A* **2015**, 3, 4909–4915.
- (11) Zhang, J.; Pauporté, T. Effects of Oxide Contact Layer on the Preparation and Properties of CH₃NH₃PbI₃ for Perovskite Solar Cell Application. *J. Phys. Chem. C* **2015**, 119, 14919–14928.
- (12) Zhang, J.; Pauporté, T. One-Dimensional Self-Standing TiO₂ Nanotube Array Layers Designed for Perovskite Solar Cell Applications. *ChemPhysChem* **2015**, 16, 2836–2841.

T. Zhu, D. Zheng, J. Liu, L. Coolen, Th. Pauporté, *ACS Appl. Mater. Interfaces* 12 (2020) 37197–37207

- (13) Tu, Y. G.; Xu, G. N.; Yang, X. Y.; Zhang Y. F.; Li, Z. J.; Su R.; Luo D. Y.; Yang, W. Q.; Miao, Y.; Cai R.; Jiang L. H.; Du, X. W.; Yang, Y. C.; Liu, Q. S.; Gao, Y.; Zhao, S.; Huang, W.; Gong, Q. H.; Zhu, R. Mixed-Cation Perovskite Solar Cells in Space. *Sci. China-Phys. Mech. Astron.* **2019**, *62*, 974221.
- (14) Yang, W. S.; Park, B. W.; Jung, E. H.; Jeon, N. J.; Kim, Y. C.; Lee, D. U.; Shin, S. S.; Seo, J.; Kim, E. K.; Noh, J. H.; Seok, S. I. Iodide Management in Formamidinium-Lead-Halide-Based Perovskite Layers for Efficient Solar Cells. *Science* **2017**, *356*, 1376–1379.
- (15) Leblanc, A.; Mercier, N.; Allain, M.; Dittmer, J.; Fernandez, V.; Pauporté, T. Lead-and Iodide-Deficient (CH₃NH₃)PbI₃ (d-MAPI): the Bridge between 2D and 3D Hybrid Perovskites. *Angew. Chem., Int. Ed.* **2017**, *56*, 16067–16072.
- (16) Wang, P.; Shao, Z.; Ulfa, M.; Pauporté, T. Insights into the Hole Blocking Layer Effect on the Perovskite Solar Cell Performance and Impedance Response. *J. Phys. Chem. C* **2017**, *121*, 9131–9141.
- (17) Wang, P.; Ulfa, M.; Pauporté, T. Effects of Perovskite Monovalent Cation Composition on the High and Low Frequency Impedance Response of Efficient Solar Cells. *J. Phys. Chem. C* **2018**, *122*, 1973–1981.
- (18) Turren-Cruz, S. H.; Hagfeldt, A.; Saliba, M. Methylammonium-Free, High-Performance, and Stable Perovskite Solar Cells on a Planar Architecture. *Science* **2018**, *362*, 449–453.
- (19) NREL chart (2020) <https://www.nrel.gov/pv/cell-efficiency.html>
- (20) Leijtens, T.; Eperon, G. E.; Noel, N. K.; Habisreutinger, S. N.; Petrozza, A.; Snaith, H. J. Stability of Metal Halide Perovskite Solar Cells. *Adv. Energy. Mater.* **2015**, *5*, 1500963.
- (21) Jeon, N. J.; Na, H.; Jung, E. H.; Yang, T. Y.; Lee, Y. G.; Kim, G.; Shim, H. W.; Seok, S. I.; Lee, J.; Seo, J. A Fluorene-Terminated Hole-Transporting Material for Highly Efficient and Stable Perovskite Solar Cells. *Nat. Energy* **2018**, *3*, 682–689.
- (22) Jiang, Q.; Zhao, Y.; Zhang, X.; Yang, X.; Chen, Y.; Chu, Z.; Ye, Q.; Li, X.; Yin, Z.; You, J. Surface Passivation of Perovskite Film for Efficient Solar Cells. *Nat. Photonics* **2019**, *13*, 460–466.

T. Zhu, D. Zheng, J. Liu, L. Coolen, Th. Pauporté, *ACS Appl. Mater. Interfaces* 12 (2020) 37197–37207

- (23) Jung, E. H.; Jeon, N. J.; Park, E. Y.; Moon, C. S.; Shin, T. J.; Yang, T. Y.; Noh, J. H.; Seo, J. Efficient, Stable and Scalable Perovskite Solar Cells Using Poly (3-Hexylthiophene). *Nature* **2019**, 567, 511-515.
- (24) Yoo, J. J.; Wieghold, S.; Sponseller, M. C.; Chua, M. R.; Bertram, S. N.; Hartono, N.T.P.; Tresback, J. S.; Hansen, E. C.; Correa-Baena, J. P.; Bulović, V.; Buonassisi, T.; An Interface Stabilized Perovskite Solar Cell with High Stabilized Efficiency and Low Voltage Loss. *Energy Environ. Sci.* **2019**, 12, 2192–2199.
- (25) Liu, Y.; Akin, S.; Pan, L.; Uchida, R.; Arora, N.; Milić, J. V.; Hinderhofer, A.; Schreiber, F.; Uhl, A. R.; Zakeeruddin, S. M.; Hagfeldt, A.; Dar, M. I.; Gratzel, M. Ultrahydrophobic 3D/2D Fluoroarene Bilayer-Based Water-Resistant Perovskite Solar Cells with Efficiencies Exceeding 22%. *Sci. Adv.* **2019**, 5, eaaw2543.
- (26) Kim, M.; Kim, G. H.; Lee, T. K.; Choi, I. W.; Choi, H. W.; Jo, Y.; Yoon, Y. J.; Kim, J. W.; Lee, J.; Huh, D.; Lee, H.; Kwak, S. K. Kim, J. Y.; Kim, D. S. Methylammonium Chloride Induces Intermediate Phase Stabilization for Efficient Perovskite Solar Cells. *Joule* **2019**, 3, 1–14.
- (27) Zhu, T.; Su, J.; Labat, F.; Ciofini, I.; Pauporté T. Interfacial Engineering through Chloride-Functionalized Self-Assembled Monolayer for High Efficiency Perovskite Solar Cells. *ACS Appl. Mater Interfaces*, **2020**, 12, 744–752.
- (28) Edri, E.; Kirmayer, S.; Mukhopadhyay, S.; Gartsman, K.; Hodes, G.; Cahen, D. Elucidating the Charge Carrier Separation and Working Mechanism of $\text{CH}_3\text{NH}_3\text{PbI}_{3-x}\text{Cl}_x$ Perovskite Solar Cells. *Nature Commun.* **2014**, 5, 3461.
- (29) Buin, A.; Pietsch, P.; Xu, J.; Voznyy, O.; Ip, A. H.; Comin, R.; Sargent, E. H. Materials Processing Routes to Trap-Free Halide Perovskites. *Nano Lett.* **2014**, 14, 6281–6286.
- (30) Mu, C.; Pan, J.; Feng, S.; Li, Q.; Xu, D. Quantitative Doping of Chlorine in Formamidinium Lead Trihalide ($\text{FAPbI}_{3-x}\text{Cl}_x$) for Planar Heterojunction Perovskite Solar Cells. *Adv. Energy Mater.* **2017**, 7, 1601297.
- (31) Jeon, N. J.; Na, H.; Jung, E. H.; Yang, T. Y.; Lee, Y. G.; Kim, G.; Shin, H. -W.; Seok, S. I.; Lee, J.; Seo, J. A Fluorene-Terminated Hole-Transporting Material for Highly Efficient and Stable Perovskite Solar Cells. *Nat. Energy* **2018**, 3, 682–689.

T. Zhu, D. Zheng, J. Liu, L. Coolen, Th. Pauporté, *ACS Appl. Mater. Interfaces* 12 (2020) 37197–37207

- (32) Cho, K. T.; Grancini, G.; Lee, Y.; Oveisi, E.; Ryu, J.; Almora, O.; Tschumi, M.; Schouwink, P. A.; Seo, G.; Heo, S.; Park, J.; Jang, J.; Paek, S.; Garcia-Belmonte G. and Nazeeruddin, M. K. Selective Growth of Layered Perovskites for Stable and Efficient Photovoltaics. *Energy Environ. Sci.* **2018**, *11*, 952–959.
- (33) Xie, F.; Chen, C. C.; Wu, Y.; Li, X.; Cai, M.; Liu, X.; Yang, X.; Han, L. Vertical Recrystallization for Highly Efficient and Stable Formamidinium-Based Inverted-Structure Perovskite Solar Cells. *Energy Environ. Sci.* **2017**, *10*, 1942–1949.
- (34) Wu, Y. -H.; Ding, Y.; Liu, X. -Y.; Pan, X.; Wu, J. -H.; Dai, S. -Y. Sequential Processing: Crystallization of Ultra smooth $\text{FA}_{1-x}\text{MA}_x\text{PbI}_3$ Perovskite Layers for Highly Efficient and Stable Planar Solar Cells. *Sol. RRL* **2020**, *4*, 1900183.
- (35) Mateen, M.; Arain, Z.; Yang, Y.; Liu, X.; Ma, S.; Liu, C.; Ding, Y.; Ding, X.; Cai M.; Dai, S. MAI-Induced Intermediate Engineering for High-Performance Mixed-Cation Perovskite Solar Cells. *ACS Appl. Mater. Interfaces* **2020**, *12*, 10535–10543.
- (36) Kim, G. M.; Ishii, A.; Öz, S.; Miyasaka, T. MAI-Assisted Ge Doping of Pb-Hybrid Perovskite: A Universal Route to Stabilize High Performance Perovskite Solar Cells. *Adv. Energy Mater.* **2020**, *10*, 1903299.
- (37) Lee, J. -W.; Dai, Z.; Han, T. -H.; Choi, C.; Chang, S. -Y.; Lee, S. -J.; De Marco, N.; Zhao, H.; Sun, P.; Huang Y.; Yang, Y. 2D Perovskite Stabilized Phase-Pure Formamidinium Perovskite Solar Cells. *Nat. commun.* **2018**, *9*, 3021.
- (38) Quan, L. N.; Yuan, M.; Comin, R.; Voznyy, O.; Beauregard, E. M.; Hoogland, S.; Buin, A.; Kirmani, A. R.; Zhao, K.; Amassian, A.; Kim, D. H.; Sargent, E. H. Ligand-Stabilized Reduced-Dimensionality Perovskites. *J. Am. Chem. Soc.* **2016**, *138*, 2649–2655.
- (39) Tress, W.; Yavari, M.; Domanski, K.; Yadav, P.; Niesen, B.; Baena, J.P.C.; Hagfeldt, A.; Graetzel, M. Interpretation and Evolution of Open-Circuit Voltage, Recombination, Ideality Factor and Subgap Defect States During Reversible Light-Soaking and Irreversible Degradation of Perovskite Solar Cells. *Energy Environ. Sci.* **2018**, *11*, 151–165.
- (40) Ulfa, M.; Zhu, T.; Goubard, F.; Pauporté, T. Molecular Versus Polymeric Hole Transporting Materials for Perovskite Solar Cell Application. *J. Mater. Chem. A* **2018**, *6*, 13350–13358.

T. Zhu, D. Zheng, J. Liu, L. Coolen, Th. Pauporté, *ACS Appl. Mater. Interfaces* 12 (2020) 37197–37207

- (41) Jacobs, D. A.; Shen, H.; Pfeffer, F.; Peng, J.; White, T. P.; Beck, F.J.; Catchpole, K.R. The Two Faces of Capacitance: New Interpretations for Electrical Impedance Measurements of Perovskite Solar Cells and Their Relation to Hysteresis. *J. Appl. Phys.* **2018**, *124*, 225702.
- (42) Pitarch-Tena, D.; Ngo, T.T.; Vallés-Pelarda, M.; Pauporté, Th.; Mora-Seró, I. Impedance Spectroscopy Measurements in Perovskite Solar Cells. Device Stability During the Measurement and Noise Reduction. *ACS Energy Lett.* **2018**, *3*, 1044–1048.
- (43) Ulfa, M.; Wang, P.; Zhang, J.; Liu, J.; de Marcillac, W. D.; Coolen, L.; Peralta, S.; Pauporté, T. Charge Injection and Electrical Response in Low-Temperature SnO₂-Based Efficient Perovskite Solar Cells. *ACS Appl. Mater. Interfaces* **2018**, *10*, 35118–35128.
- (44) Ulfa, M.; Pauporté, T.; Bui, T.T.; Goubard, F. Impact of Organic Hole Transporting Material and Doping on the Electrical Response of Perovskite Solar Cells. *J. Phys. Chem. C.* **2018**, *122*, 11651–11658.
- (45) Guerrero, A.; Juarez-Perez, E. J.; Bisquert, J.; Mora-Sero I.; Garcia-Belmonte, G. Electrical Field Profile and Doping in Planar Lead Halide Perovskite Solar Cells. *Appl. Phys. Lett.* **2014**, *105*, 133902.
- (46) Jiang, C. -S.; Yang, M.; Zhou, Y.; To, B.; Nanayakkara, S. U.; Luther, J. M.; Zhou, W.; Berry, J. J.; van de Lagemaat, J.; Padture, N. P.; Zhu, K.; Al-Jassim, M. M. Carrier Separation and Transport in Perovskite Solar Cells Studied by Nanometre-Scale Profiling of Electrical Potential. *Nat. Commun.* **2015**, *6*, 8397.
- (47) Almora, O.; Aranda, C.; Mas-Marzá, E. and Garcia-Belmonte, G. On Mott-Schottky Analysis Interpretation of Capacitance Measurements in Organometal Perovskite Solar Cells. *Appl. Phys. Lett.* **2016**, *109*, 173903.
- (48) Ulfa, M.; Wang, P.; Shao, Z.; Viana, B.; Pauporté, T. Oxide Hole Blocking Selective Contacts in Perovskite Solar Cells. *Proc. SPIE* **2018**, *10533*, 105332R1–105332R10.
- (49) Le Bahers, T.; Labat, F.; Pauporté T.; Ciofini, I. Effect of Solvent and Additives on the Open-Circuit Voltage of ZnO-Based Dye-Sensitized Solar Cells: A Combined Theoretical and Experimental Study. *Phys. Chem. Chem. Phys.* **2010**, *12*, 14710–14719.

T. Zhu, D. Zheng, J. Liu, L. Coolen, Th. Pauporté, *ACS Appl. Mater. Interfaces* 12 (2020) 37197–37207

- (50) Kusumawati, Y.; Martoprawiro, M. A.; Pauporté, T. Effects of Graphene in Graphene/TiO₂ Composite Films Applied to Solar Cell Photoelectrode. *J. Phys. Chem. C* **2014**, *118*, 9974–9981.

TOC Graphic

